Flight control using pin-protuberances for blunted cones

R. Samar **S. Zahir** **M. A. Khan**
raza@mail.comsats.net.pk **cfdpak@apollo.net.pk**
National Engineering and Scientific Commission
Islamabad, Pakistan

ABSTRACT

This paper presents the concept of using cylindrical pins as short protuberances for trajectory control of a blunted cone in the supersonic and hypersonic regimes. Supersonic and hypersonic flow interactions for cylindrical protuberances, installed on a blunt cone are studied for their aerodynamic effects. The utility of these protuberances for aerodynamic control and trajectory shaping of a re-entry cone are explored. Static aerodynamic coefficients in the Mach range of 2–9·7 at various incidences are computed. The pressure distribution along the vehicle longitudinal axis in the presence of the pin-protuberance is studied using CFD analysis. With the altered pressure distribution, a net increase in the aerodynamic force is obtained which can be actively utilised for flight control and maneuvering of the vehicle during re-entry. After quantifying the aerodynamic effects of the protuberance, it is modelled and used as an effective actuation mechanism for flight feedback control. It is shown that this can work as an effective control device for Mach numbers less than five. An actuator design for insertion/retraction of the protuberance is presented and modelled, and a robust controller is synthesised which can in real time govern the position of the protuberance to control the flight attitude angle to achieve a desired trajectory. The controller takes in measurements of the vehicle's pitch angle and actuates the pin height continuously to control the pitch angle to a desired value. The control performance is demonstrated on a high fidelity six degrees-of-freedom (6-DOF) nonlinear flight simulation.

NOMENCLATURE

α, β	the angles-of-attack and sideslip of the vehicle (the trim angle of attack is assumed to be zero)
$\bar{h}$	actuator planetary roller screw lead
δ_c, δ_{cref}	actual and commanded (or reference) actuator displacements
ρ	the density of air
θ	the perturbation pitch angle (small scale deviation around the equilibrium pitch angle)
Θ, φ, ψ	the pitch, roll and yaw Euler angles relating the body attitude wrt an inertial frame, respectively
$\vartheta, \vartheta s$	actuator motor shaft rotation angle, actuator roller screw rotation angle
C_x, C_z, C_m	the aerodynamic force and moment coefficients
$C_{m\delta c}$	the pitching moment control derivative coefficient
$C_{z\delta c}$	the Z-force control derivative coefficient
D, H	the diameter and height (extension) of the cylindrical pin-protuberance
e_i	control voltage applied to the actuator motor
g	the acceleration due to gravity
h	the altitude of the vehicle
i_0	actuator motor no-load current
i_a	actuator motor armature current
I_x, I_y, I_z	the principal moments of inertia of the vehicle about the body axes
J_m, B_m	moment of inertia of actuator motor armature plus load, viscous damping coefficient of actuator rotating assembly
k_a	actuator motor torque constant
k_p, k_I, k_D	proportional, integral and derivative gains of the actuator PID controller

Paper No. 3439. Manuscript received 31 March 2009, revised version received 6 July 2009 accepted 3 December 2009.

https://doi.org/10.1017/S0001924000003699 Published online by Cambridge University Press

L, M, N the components of the net moment acting on the vehicle in the body frame
m the mass of the vehicle
n_1, n actuator gear ratio, actuator overall deceleration constant
p, q, r the components of the angular velocity vector of the vehicle in the body frame (the roll, pitch and yaw body rates, respectively)
p_N, p_E the north and east position of the vehicle
P_{ref} reference pressure used for normalisation, taken as 34·8kPa for this study (this is the static pressure at an altitude of 8km)
q_∞ the free-stream dynamic pressure
R_a, L_a actuator motor armature resistance and winding inductance
S, L_{ref} the reference area and the reference length for computation of aerodynamic forces and moments from non-dimensional coefficients
T_m, T_f actuator motor torque, actuator friction torque
U, V, W the components of the velocity vector of the vehicle in the body frame
V_T the total velocity $(= \sqrt{U^2 + V^2 + W^2})$
X, Y, Z the components of the net force acting on the vehicle in the body frame
X_c, Z_c, M_c the force and moment components due to control actuation
X_p, Z_p, M_p the force and moment components due to the propulsion source

1.0 INTRODUCTION

Aerodynamic control of aerospace vehicles including both missiles and guided projectiles that operate in the high supersonic to hypersonic range, utilising mechanical devices such as those producing short protuberances, is gaining interest. For instance, the HyFly project of the Office of Naval Research[6] is a Mach 6 vehicle designed for use against targets of opportunity employing pin-protuberances. Other applications of interest using protuberance devices include cruise missile defense systems, such as the Defense Advanced Research Projects Agency's (DARPA's) low cost cruise missile defense program, and the US Army's enhanced area air defense system. One candidate defense system is based on a medium caliber gun with a high fire-rate which could possibly fire multiple supersonic guided projectiles into an incoming missile undergoing evasive maneuvers[18]. Historically much of the initial work on control devices for aerodynamic vehicles was based on reaction control jets (RCJs), these have also been considered for small guided projectiles[7]. The nature of these studies was to examine the impact of RCJs on the overall flow-field around the body; since then various parameters of RCJs have been experimentally explored such as the effect on control performance of pressure ratio, gas temperature, injection port geometry, injection port orientation and location, flight Mach number, etc[2]. On the other hand, work has also been performed by replacing jets with solid pins or obstacles[8,19,20,21,22,23].

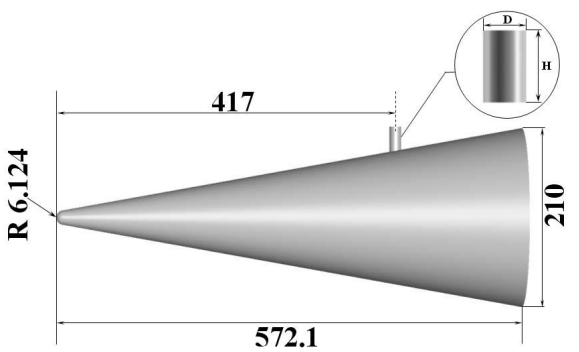


Figure 1. Blunted cone configuration with pin protuberance (all dimensions in mm).

This paper presents the aerodynamic analysis of a short cylindrical pin-protuberance on a blunt body, with a special emphasis on the effectiveness of the pin as a possible means of re-entry trajectory control. The study is extended here to hypersonic flows, ranging from Mach 2–9·7 at various incidences. The height of the cylindrical protuberance is varied from zero (flush with the vehicle's surface) to twice the diameter of the pin. The flow is analysed using pressure contours and velocity vector plots. Computational fluid dynamics (CFD) calculations are made using the Navier Stokes solver PAK-3D[5]; all post-processing is performed using the post-processing software LOOK[4]. After quantifying the control effectiveness of the protuberance at different Mach numbers and incidence angles, an actuator design is proposed which can be used to actuate the protuberance height to a desired value. The actuator design is presented and its dynamics are modelled. The equations of motion of the vehicle are presented and the dynamic model of the vehicle including the actuator is developed. A robust controller is then synthesised which controls the pitch attitude of the vehicle by actuating the protuberance height during the re-entry phase of the vehicle's flight. The controller is implemented in the nonlinear six degrees-of-freedom (6-DOF) flight simulation and its performance is tested against different commanded pitch angle profiles. The main contribution of the paper is to quantify the control effectiveness of the pin-protuberance for a blunted cone configuration for different Mach numbers, and then develop a trajectory control system based on this concept.

This paper is organised as follows. Section 2 formulates the problem and defines the vehicle configuration characteristics. Section 3 describes the computational fluid dynamics study of the vehicle with the pin-protuberance, and discusses its aerodynamic characteristics. Effects of varying the protuberance height and the Mach number are discussed. The dynamical equations of motion of the vehicle and the actuation mechanism are developed in Section 4. Section 5 details a robust controller design methodology and presents the design of a controller based on H_∞ theory. The controller takes in measurements of the vehicle's pitch angle and actuates the pin height continuously to control the pitch angle to a desired value. Flight simulation results with the controller in the loop are presented in Section 6. Finally Section 7 concludes the paper.

Table 1
Re-entry vehicle (blunted cone) configuration characteristics

Parameter	Value
Nose radius	6·124mm
Base radius	105mm
Reference Length, L_{ref}	572·1mm
Mass, m	50kg
Length, L	572·1mm
Reference area, S	0·03463m^2
Pitch/Yaw moment of inertia, I_y	1·5kg-m^2
Centre of gravity location from nose, X_{cg}/L	0·5945
Centre of pressure location from nose, X_{cp}/L	0·63
Pitching moment derivative, $C_{m\alpha}$	−0·0013 per degree
Z-force derivative, $C_{z\alpha}$	−0·0329 per degree
Pitch damping force coefficient, C_{zq}	0·36 per rad
Pitch damping moment coefficient, C_{mq}	−0·44 per rad
Control pin diameter, D	14·2mm
Control pin extension, H	0–28·4mm
Control pin location (from nose)	417mm

https://doi.org/10.1017/S0001924000003699 Published online by Cambridge University Press

2.0 PROBLEM FORMULATION

In the present study, the selected model is a blunted cone configuration having a half-cone angle of 10·4°. The base diameter is 210mm, and the cylindrical pin is located at a distance of 417mm from the blunted nose. The diameter D of the pin is 14·2mm, and the protruded height H of the pin can be varied from zero (flushed with the surface) to twice its diameter. Geometrical details of the configuration are as shown in Fig. 1. The basic physical characteristics of the vehicle are given in Table 1.

Traditionally re-entry vehicles of this type are spun upon release from the parent craft and undergo a ballistic uncontrolled flight from there on. Along-track and cross-track errors may however arise because of various sources, such as uncertainty in the separation impulse upon release from the carrier vehicle, aerodynamic and mass asymmetries (this may yield to complex dynamical phenomena, such as roll resonance and lock-in), wind disturbances, uncertainty in the knowledge of aerodynamic drag of the vehicle, etc. Precise positioning requirements dictate the need for a trajectory control system which remains active till the terminal phase of the vehicle's flight. Such a terminal control philosophy will require high fidelity sensors which can provide accurate position and velocity measurements for navigation and guidance, as well as good attitude information for feedback control. Here we require the vehicle to have a roll control system and it is assumed that such a system is available (perhaps thruster based) which keeps the vehicle roll angle at zero. Typically the overall guidance and control system will be a multi-loop system with the outer guidance loop looking at the vehicle's position and velocity, comparing it with the desired trajectory and generating guidance commands. These guidance commands will be in the form of desired pitch and yaw angles which the inner attitude control loops will be designed to track.

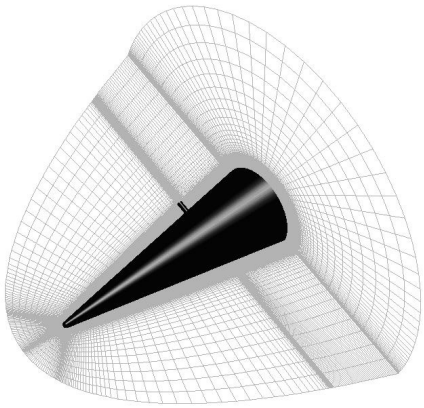
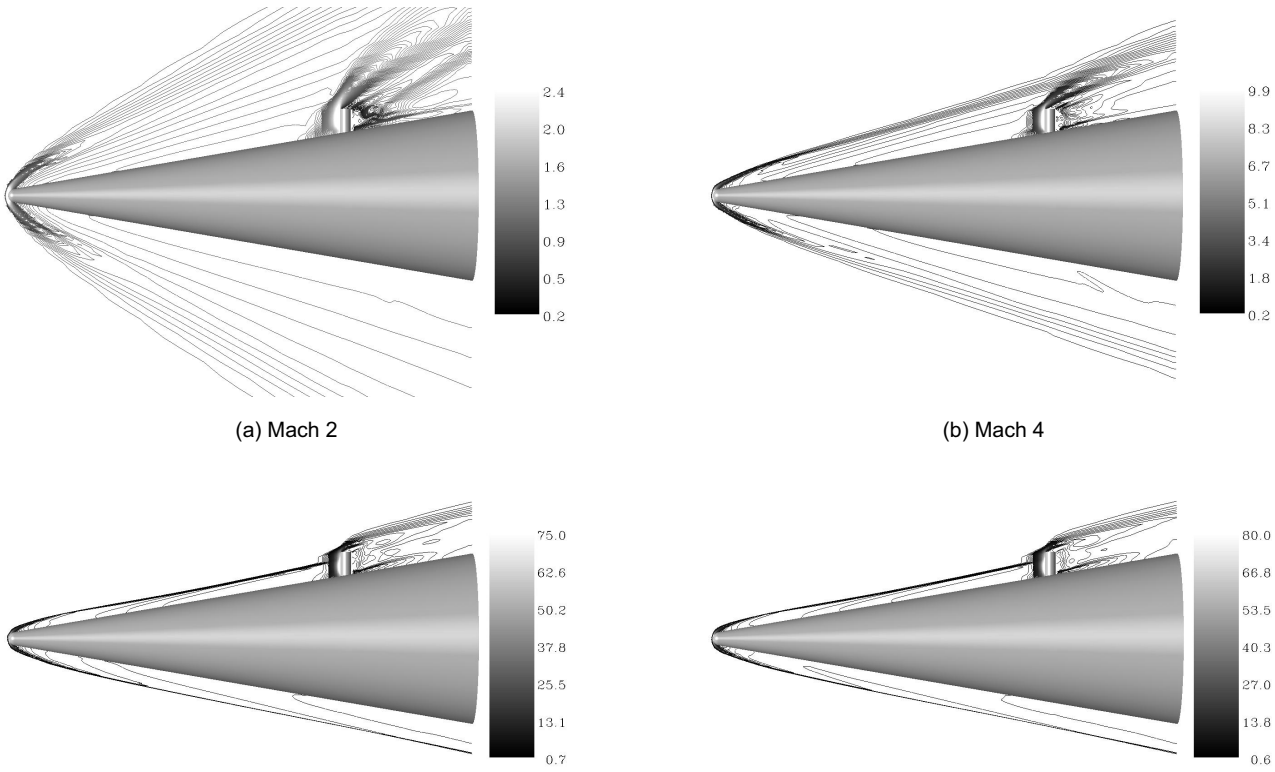


Figure 2. Grid for the short cylindrical pin-protuberance installed on the blunted cone.

It is envisaged that for longitudinal and lateral plane guidance, a set of four pin-protuberance mechanisms, 90° apart will be required. The top pin will be actuated to produce a nose-down moment (which then generates a negative angle-of-attack), and the bottom pin will be actuated to produce a nose-up moment. Similarly the two side pins will provide yawing moments and hence generate sideslip angles for lateral guidance.

Using pin-protuberances for control is a relatively new idea; traditionally thrusters have been used, however there are pros and cons of both concepts. Typically thrusters provide on-off (bang-bang) control while the pin-protuberance provides continuous proportional



(a) Mach 2

(b) Mach 4

(c) Mach 6

(d) Mach 9·7

Figure 3. Normalised pressure distribution (P/P_{ref}) contours for different Mach numbers, $\alpha = -2^{\circ}$, $H = 2D$.

https://doi.org/10.1017/S0001924000003699 Published online by Cambridge University Press

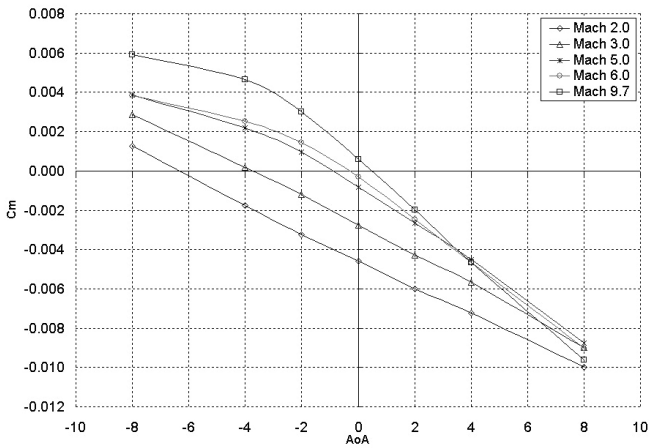


Figure 4. C_m variation with angle of attack for different Mach numbers for $H = 2D$.

control. Thrusters need a complex, expensive and bulky feed system employing high pressure bottles, solenoid valves, pipings and other accessories. Also thrusters are designed to operate optimally at a given ambient pressure, an increase in this pressure (because of lower altitudes, for example) will reduce the thrust generated. The pin-protuberance on the other hand cannot work in very rare atmosphere (at very low dynamic pressures) as it relies on aerodynamic forces as opposed to pure jet momentum. The two actuation systems may even be optimally combined to get the best advantage from each in different phases of a vehicle's flight.

The problem under study here is to use this generic re-entry vehicle (which is a blunted cone configuration with a controllable pin extension mechanisms) to investigate the feasibility of the pin protuberance for closed-loop trajectory control. We shall explore the flight envelope in which the protuberance can be effective, and then model its dynamic characteristics. We shall also design control laws using the variable extension protuberance as a control actuation mechanism for vehicle attitude control. The control law will be implemented in a nonlinear flight simulation, and results will be discussed.

3.0 COMPUTATIONAL FLUID DYNAMICS

3.1 Grid generation

The computational grid quality with regards to its density and packing, required for capturing flow details in the supersonic and hypersonic regimes (Mach 2 to 9·7) and satisfactory convergence is derived from earlier studies[20,21]. Since the vehicle is symmetric, a structured 180-degree grid is generated. A typical grid used for Mach 9·7 computations for a protuberance height of twice the diameter ($H = 2D$), consists of four blocks and 0·106 million cells; see Fig. 2. The minimum spacing of the grid close to the pin is 0·08mm (radially outward), which is much smaller than the boundary-layer thickness for Mach 9·7. Grid packing over the pin is dense; 55 points are taken on the pin along its axis, and 100 along its circumference.

Flow computations are made using a full Navier Stokes solver[5] which uses implicit diagonalised Beam-Warming numerics with fourth order artificial viscosity dissipation. Several turbulence models (e.g., Baldwin-Lomax and Chien's k-ε) are available. Boundary conditions are applied at the outer computational boundaries and at relevant embedded surfaces.

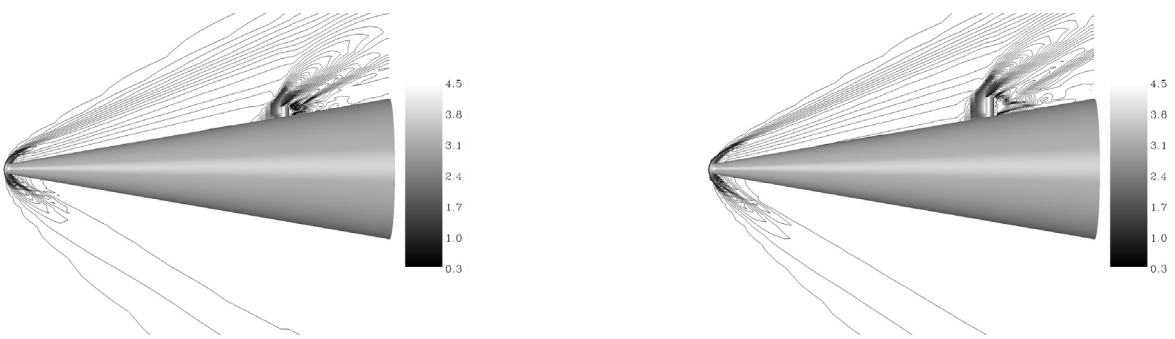
3.2 Boundary conditions

Appropriate supersonic/hypersonic inflow conditions for a half-body, 180-degree grid are used. The extrapolation condition is applied at the outlet section, while the symmetric condition is employed at the symmetry plane, and a no-slip adiabatic condition is imposed at the body surface and on the pin-protuberance. Computations are performed with the Mach number varying from 2–9·7 with angle-of-attack settings of 0, ±2, ±4 and ±8 degrees. The air specific heat ratio is taken as 1·4, and the Reynolds number ranges from $2{\cdot}8 \times 10^6$ – $1{\cdot}20 \times 10^7$. The numerical modelling of the projectile's environment during re-entry is done with the Mach and Reynolds number similitude; static aerodynamic coefficients thus computed provide sufficient accuracy for autopilot and controller design[3,21,8].

3.3 Aerodynamic characteristics

3.3.1 *Effect* of Mach number variation

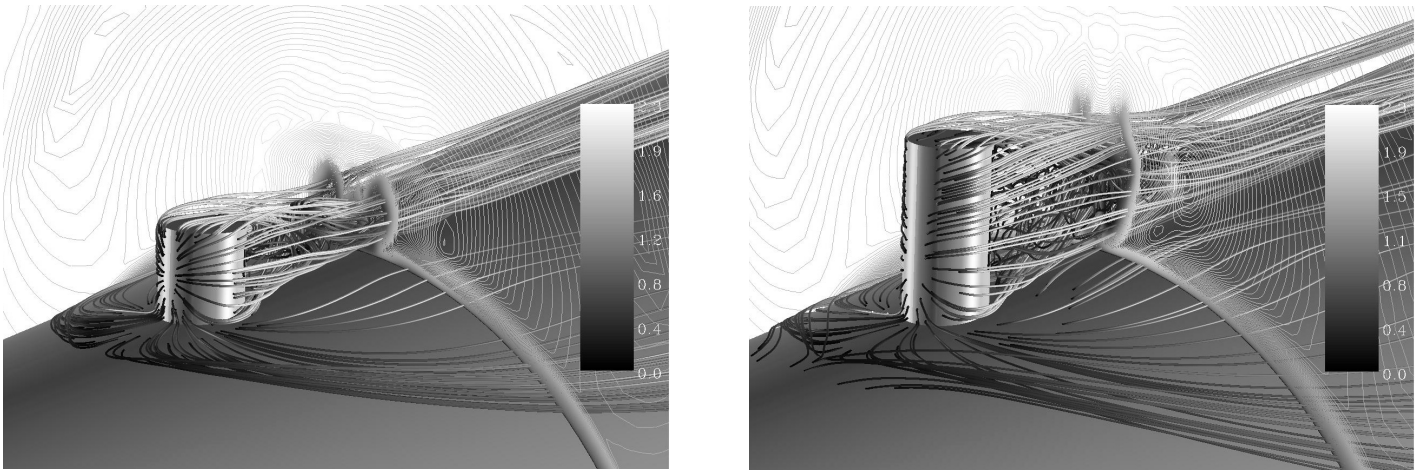
A solid pin in a supersonic flow provides blockage to the flow, its influence is felt upstream as the boundary layer thickens leading to an upstream separation shock. The pin-protuberance also causes a downstream low pressure re-circulation zone. This is seen in Fig. 3 which shows the normalised pressure distribution plots for different Mach numbers (at an incidence of −2° and for $H = 2D$), where the normalisation is done with a reference pressure $P_{ref} = 34{\cdot}8$kPa. From the pressure distribution plots, it is observed that as the Mach number increases, the bow shock from the nose interacts more strongly with the cylindrical pin-protuberance. Also the stagnation pressure on the pin increases with an increase in Mach number (the normalised pressure increases from 2·4 to 80). This pressure increase on the top side causes an increase in the differential pressure over the surface of the cone, hence resulting in an increase in the normal force.



(a) $H = D$ (b) $H = 2D$

Figure 5. Normalised pressure contours at Mach 2, $\alpha = -8°$ for $H = D$ and $H = 2D$.

https://doi.org/10.1017/S0001924000003699 Published online by Cambridge University Press



(a) $H = D$ (b) $H = 2D$

Figure 6. Streamlines and Mach contours in the vicinity of the pin at Mach 2, $\alpha = -8°$ for $H = D$ and $H = 2D$.

The static pitching moment coefficient about the centre of gravity of the vehicle for different Mach numbers (at a fixed control pin setting of $H = 2D$), indicates that the control authority of the pin-protuberance degrades with increasing Mach, and then changes sign after Mach 6. The variation of the pitching moment coefficient C_m with angle-of-attack for different Mach numbers is shown in Fig. 4. From the figure we see that the control pin can generate a trim angle of attack of −4° at Mach 3 (since at Mach 3 the configuration trims, or equivalently C_m is zero, at $\alpha \approx -4°$ with $H = 2D$). As the Mach number increases the control authority erodes and almost vanishes at Mach 6 (for the particular geometry under study here). This variation in the pitch trim capability of the pin is the net effect of the change in the normal force coefficient and the centre of pressure of the vehicle with Mach number. The plot shows that the useful range of operation of the control pin is below Mach 5 for our case.

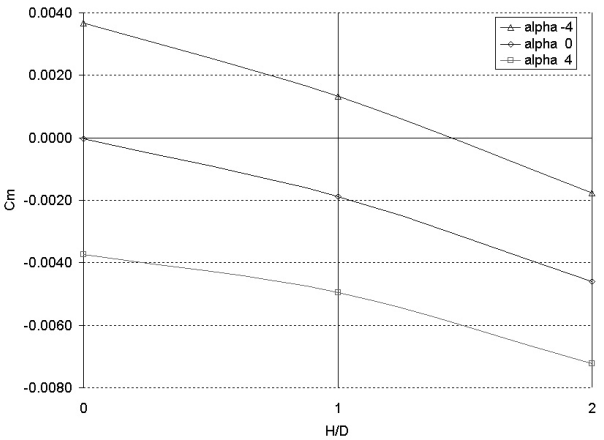


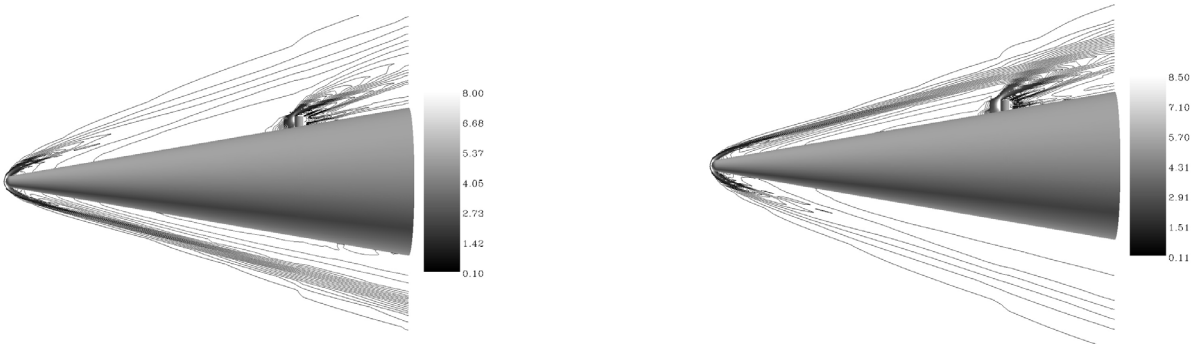
Figure 7. Plot of C_m *versus* H for different α values at Mach 2.

3.3.2 *Effect of varying the protuberance height*

It is desirable to have a linear relationship between the protuberance height and the corresponding pitching moment which it generates for control. The disturbance generated as the protuberance is introduced into the flow is a complex phenomenon, however the pressure and Mach contours and the associated streamlines in the vicinity of the pin provide useful insight. Pressure and Mach distribution plots with pin heights of $H = D$ and $H = 2D$ at Mach 2 and $\alpha = -8°$ are shown in Figs 5 and 6, respectively. As the increase in protuberance height causes an increase in the normal force with a corresponding increase in the pitching moment coefficient C_m. This is shown in Fig. 7 where the height of the pin-protuberance is varied from zero to $2D$ for different angles-of-attack, with the Mach number fixed at 2.

3.3.3 *Effect of angle-of-attack change*

For a fixed Mach number, the angle-of-attack variation gives rise to an interaction between the nose bow shock and the pin-protu-



(a) $\alpha = 4°$ (b) $\alpha = -4°$

Figure 8. Normalised pressure contours at Mach 4, $\alpha = \pm 4°$ with $H = D$.

https://doi.org/10.1017/S0001924000003699 Published online by Cambridge University Press

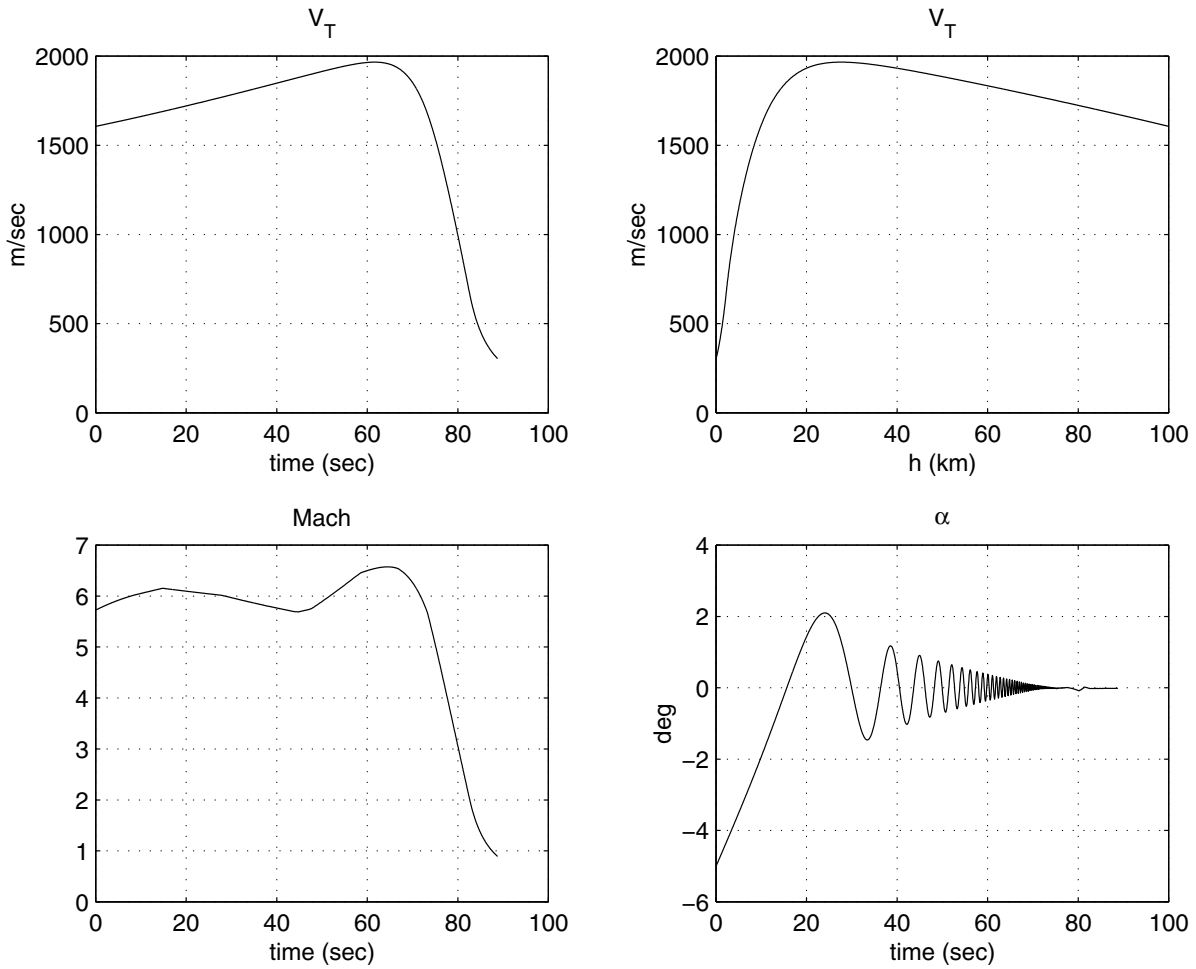


Figure 9. Free-flight simulation variables.

berance shock. For negative axngles-of-attack, maximum interaction occurs in the vicinity of the pin, therefore the axial location of the pin is important. Pressure distribution contours for angles-of-attack of −4° and +4°, at Mach 4 are shown in Fig. 8. With the pin extended upwards, negative angles-of-attack produce greater interaction of the pin with the flow, thus producing a higher normal force and pitching moment. This is good since the pin on the top (as shown) will be actuated for producing negative angles-of-attack, and as the angle of attack becomes negative the top pin becomes more effective. This is quantitatively verified from Fig. 7 where we see that the change in the pitching moment coefficient ΔC_m by varying H from 0 to $2D$ is 0·0056 for $\alpha = -4°$, but less than 0·0035 for $\alpha = +4°$.

3.3.4 Discussion

It is concluded that the short cylindrical pin-protuberance installed on the blunted cone causes an increase in the net force by altering the pressure distribution around the vehicle, with a subsequent increase in the aerodynamic pitching moment for flight behavioural control. However, in our case, the effective range where pin control can be employed is for Mach number 5 and below. Above Mach 5 the pitch control authority degrades because of the travel of the centre of pressure of the vehicle towards its centre of gravity. For effectiveness at higher Mach numbers the centre of gravity may be repositioned, but here we shall keep it unchanged.

4.0 VEHICLE DYNAMICS

4.1 Equations of motion

The standard nonlinear equations of motion describing the six degrees-of-freedom motion of a vehicle in flight are given below[16]. The force equations are:

$$\begin{aligned} \dot{U} + qW - rV &= X/m - g \sin\Theta \\ \dot{V} + rU - pW &= Y/m + g \cos\Theta \sin\phi \\ \dot{W} + pV - qU &= Z/m + g \cos\Theta \cos\phi \end{aligned} \quad \ldots (1)$$

The moment equations are:

$$\begin{aligned} I_x\dot{p} + (I_z - I_y)rq &= L \\ I_y\dot{q} + (I_x - I_z)pr &= M \\ I_z\dot{r} + (I_y - I_x)pq &= N, \end{aligned} \quad \ldots (2)$$

where we have assumed the vehicle to have a symmetric mass distribution, and have therefore neglected all cross-products of inertia. The three kinematic equations and three navigation equations complete the set:

$$\begin{aligned} \dot{\phi} &= p + \tan\Theta(q \sin\phi + r \cos\phi) \\ \dot{\Theta} &= q \cos\phi - r \sin\phi \\ \dot{\psi} &= \frac{q \sin\phi + r \cos\phi}{\cos\Theta} \end{aligned}$$

$$\dot{p}_N = U \cos\Theta \cos\psi + V(-\cos\phi \sin\psi + \sin\phi \sin\Theta \cos\psi) + W(\sin\phi \sin\psi + \cos\phi \sin\Theta \cos\psi)$$

https://doi.org/10.1017/S0001924000003699 Published online by Cambridge University Press

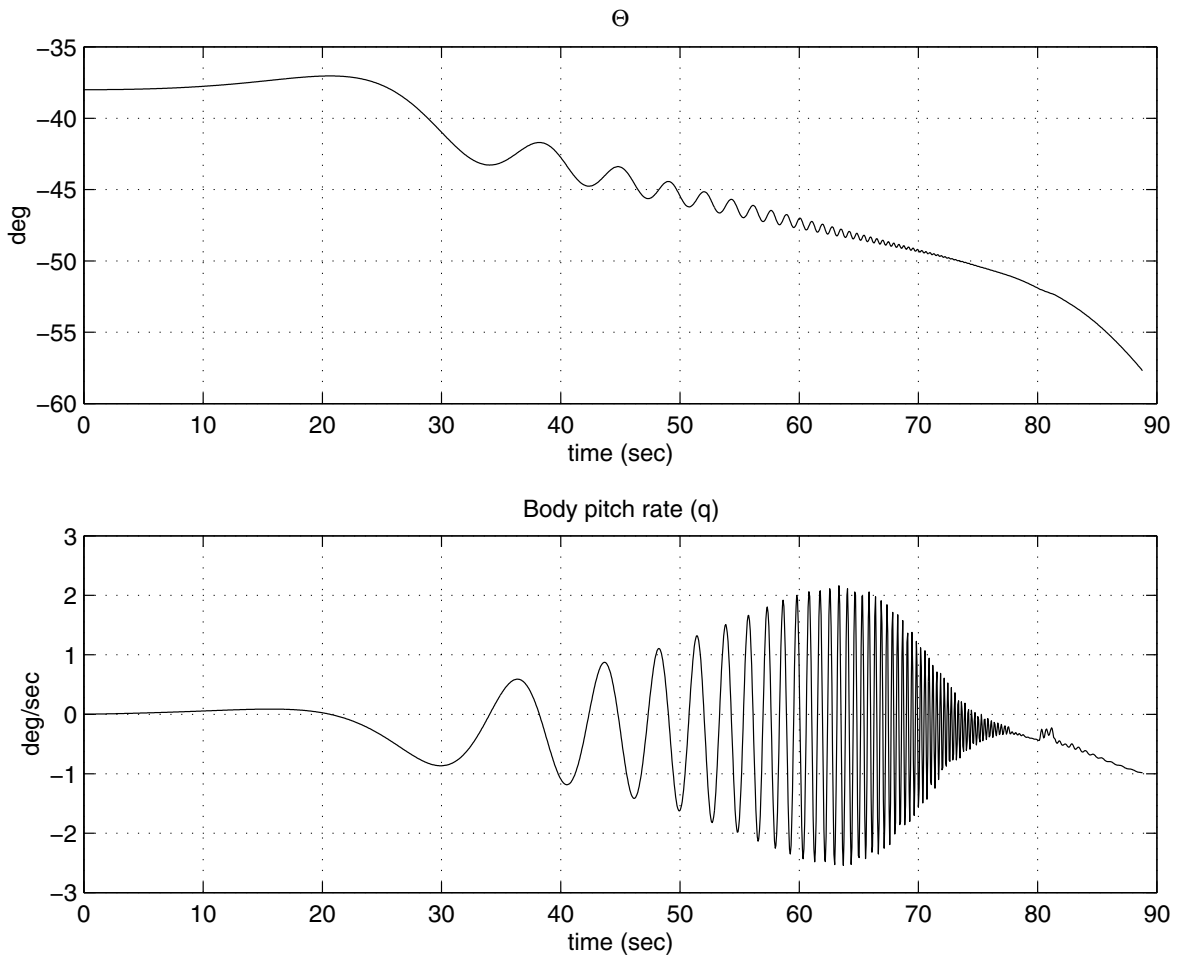


Figure 10. Free-flight simulation: pitch angle and body pitch rate.

$$\dot{p}_E = U \operatorname{Cos}\Theta \operatorname{Sin}\psi + V(\operatorname{Cos}\phi \operatorname{Cos}\psi + \operatorname{Sin}\phi \operatorname{Sin}\Theta \operatorname{Sin}\psi) + W(-\operatorname{Sin}\phi \operatorname{Cos}\psi + \operatorname{Cos}\phi \operatorname{Sin}\Theta \operatorname{Sin}\psi)$$
$$\dot{h} = U \operatorname{Sin}\Theta - V \operatorname{Sin}\phi \operatorname{Cos}\Theta - W \operatorname{Cos}\phi \operatorname{Cos}\Theta. \quad \ldots (3)$$

An alternate form of the force Equations (1) that is sometimes more convenient has the total velocity ($V_T = \sqrt{U^2 + V^2 + W^2}$), and the angles-of-attack and sideslip as state variables:

$$V_T = \frac{U\dot{U} + V\dot{V} + W\dot{W}}{V_T}$$
$$\dot{\beta} = \frac{\dot{V}V_T - V\dot{V}_T}{V_T^2 \operatorname{Cos}\beta} \quad \ldots (4)$$
$$\dot{\alpha} = \frac{U\dot{W} - W\dot{U}}{U^2 + W^2}$$

We shall assume the vehicle to have pitch and yaw mass symmetry so that $I_y = I_z$, and also the roll rate to be negligibly small. It is also assumed that the extension of the pin causes a very slight change in the moments of inertia and centre of gravity of the vehicle, which can be neglected. These assumptions shall remain in force for all our 6-DOF simulation runs.

For control law design, usually additional assumptions are taken that result in the decoupling of the longitudinal and lateral dynamical variables. Therefore we further assume that the yaw rate is negligibly small, and the initial roll angle of the vehicle is zero. Now the above equations can be separated into the longitudinal and lateral sets, the longitudinal set being:

$$\dot{U} + qW = X/m - g \operatorname{Sin}\Theta$$
$$\dot{W} - qU = Z/m + g \operatorname{Cos}\Theta \operatorname{Cos}\phi \quad \ldots (5)$$
$$I_y\dot{q} = M$$

The net forces X and Z, and the net moment M are due to the combined aerodynamic, propulsive and control effects and are non-linear functions of the angle of attack, Mach number, air density, etc:

$$X = C_x S q_\infty + X_p + X_c$$
$$Z = C_z S q_\infty + Z_p + Z_c$$
$$M = C_m S q_\infty L_{ref} + M_p + M_c.$$

A linearised (short-period) approximation to the Equations (5) can be derived; see for example[1,10], and is given below:

$$\frac{mU}{Sq_\infty}\dot{\alpha} - C_{z_\alpha}\alpha - \left(\frac{mU}{Sq_\infty} + \frac{L_{ref}}{2U}C_{zq}\right)\dot{\theta} + \frac{mg}{Sq_\infty} Sin\,\Theta\theta = C_{z_{\delta c}}\delta_c$$
$$-C_{m\alpha}\alpha + \frac{I_y}{Sq_\infty L_{ref}}\ddot{\theta} - \frac{L_{ref}}{2U}C_{m_q}\dot{\theta} = C_{m_{\delta_c}}\delta_c \quad \ldots (6)$$

Here δ_c represents the control actuation variable (which is the pin height H in our case), and $C_{z\delta c}$ and $C_{m\delta c}$ represent the control force and moment derivatives. Since the re-entry vehicle motion is mostly in hypersonic and high supersonic flow, therefore, we have neglected the flow lag derivatives $C_{m\dot{\alpha}}$ and $C_{z\dot{\alpha}}$. In hypersonic flows the translational speed of the flow is so great relative to the speed of cross flow

https://doi.org/10.1017/S0001924000003699 Published online by Cambridge University Press

induced by angular motion, that the flow adjusts nearly instantaneously to changes in cross flow. Hence both the $\dot{\alpha}$ derivatives are neglected[12].

4.2 Nonlinear simulation

We can now simulate the non-linear dynamical equations of motion (Equations 1-4). The initial conditions taken for the simulation are:

$$(V_{T0}, \beta_0, \alpha_0, q_0, \Theta_0, p_{N0}, p_{E0}, h_0)^T = (1{,}606\text{ms}^{-1}, 0°, -5°, 0\text{rad/s}, -38°, 0\text{m}, 0\text{m}, -100\text{km})^T \quad \ldots (7)$$

where the subscript '0' denotes the initial condition of the variable, and the superscript 'T' denotes the transpose of a vector or matrix. The physical characteristics of the vehicle are given in section 2. The different simulation variables of interest are plotted in Figs 9 and 10. The top left part of Fig. 9 shows the total velocity V_T plotted as a function of time with the initial time t_0 set to zero. The top right part of the same figure shows V_T plotted against altitude (as the vehicle re-enters from an altitude of 100km and finally descends to zero). The lower part of the figure shows the Mach number and the angle-of-attack α plotted against time. The static and dynamic stability of the vehicle is apparent since the angle of attack converges to zero from its initial value of −5° as the body traverses through the denser atmosphere. Figure 10 shows the pitch angle Θ and the body pitch rate q plotted against time. Figure 11 shows the variation of the dynamic pressure ($q_\infty = \frac{1}{2}\rho V_T^2$) with flight time and also with altitude.

The dynamic pressure varies greatly during re-entry and this poses a challenge for control; the controller has to perform well in the face of such largely varying dynamics.

4.3 Actuator dynamics

The actuator designed for extension/retraction of the control pin is of linear electromechanical type. It has a rated output force of 500 Newtons, a rated speed of 30mm/sec, and a maximum operational stroke of 40mm. The actuator is powered by a brushless DC motor and has a two stage decelerator mechanism, see Fig. 12. The first stage consists of three spur gears and the second stage employs a planetary roller screw (Fig. 13). The electronics section has a control circuit (also called the signal synthesising circuit), a pulse width modulator, and a power amplifier circuit that drives the motor. The control circuit synthesises and amplifies the position error signal of the actuator push-rod and provides input to the pulse width modulator. The pulse width modulator adjusts the width of the output pulses that pass through the power stage before being applied to the motor. The output pinion of the motor drives a gear train and a ball lead screw which converts the rotary motion into linear push-rod movement. A feedback potentiometer senses the linear position of the push rod which is used by the control circuit for servo control. The electrical equation of the motor is given by:

$$e_i = i_a R_a + L_a \frac{di_a}{dt} + k_a \dot{\vartheta}.$$

The rotational equation of motion is:

$$T_m = J_m \ddot{\vartheta} + B_m \dot{\vartheta},$$

where the motor torque T_m is directly proportional to the armature current: $T_m = k_a i_a$. The rotation of the screw is related to the motor shaft rotation by the gear ratio n_1: $\vartheta_s = \vartheta / n_1$. The actuator linear displacement output δ_c (which is the same as the pin height H) can

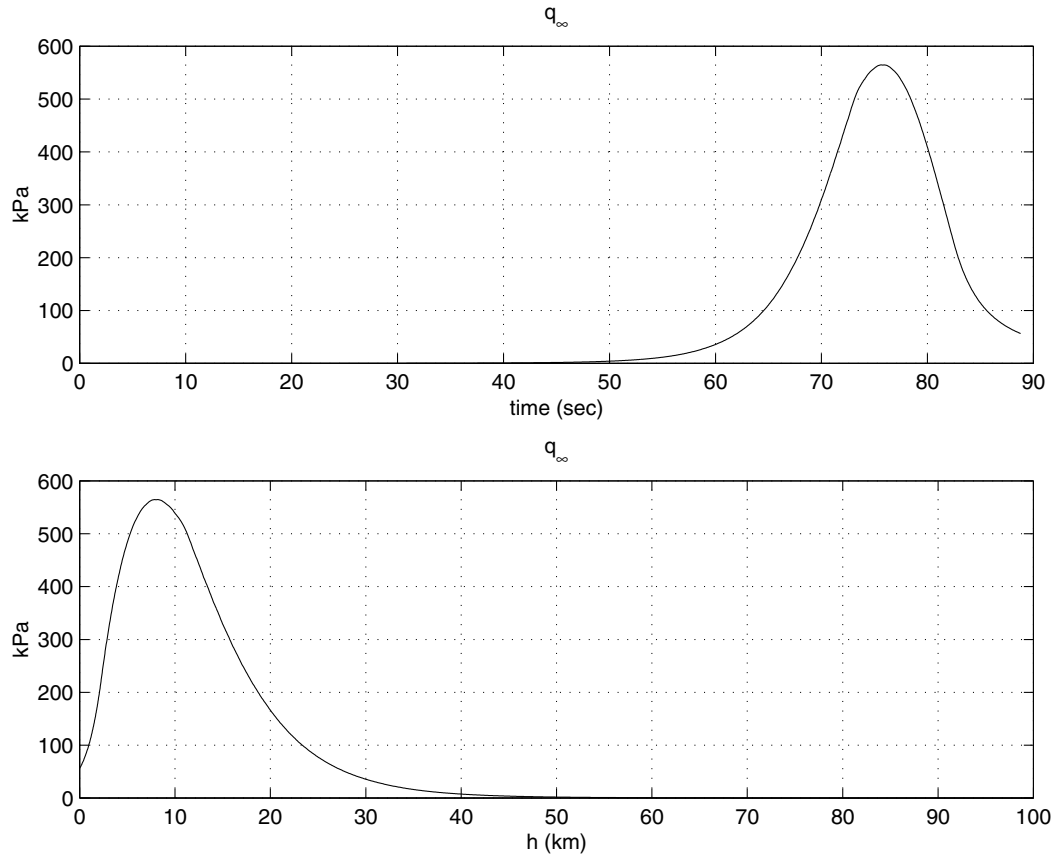


Figure 11. Dynamic pressure q_∞ during flight.

https://doi.org/10.1017/S0001924000003699 Published online by Cambridge University Press

be written as:

$$\delta_c = \frac{\bar{h}}{2\pi n_1}\vartheta = \frac{1}{n}\vartheta$$

where $\bar{h}$ is the roller screw lead and n is the actuator overall deceleration constant.

The nonlinearities in the actuator arise primarily from the voltage and current limitation in the control and drive circuits, and the friction of the moving parts. The friction torque can be modelled as $T_f = k_a i_0 \text{sgn}(\dot{\vartheta})$, where sgn(•) denotes the 'signum' or 'sign' function. Neglecting the nonlinearities for now, we can derive an open-loop transfer function of the actuator dynamics relating the displacement output δ_c to the control voltage e_i as:

$$\frac{\delta_c}{e_i} = \frac{k_a/n}{(L_a s + R_a)(J_m s^2 + B_m s) + k_a s^2}$$

where 's' denotes the Laplace variable. The actuator has a local PID controller (implemented in the signal synthesising/control circuit) with parameters k_p, k_I, k_D, so that the closed-loop actuator transfer function relating the actual actuator displacement (δ_c or H) to the commanded displacement is:

$$\frac{\delta_c}{\delta_{cref}} = \frac{k_a k_D s^2 + k_a k_p s + k_a k_I}{L_a J_m n s^4 + n(J_m R_a + L_a B_m)s^3 + (R_a B_m n + k_a^2 + k_a k_D)s^2 + k_a k_p s + k_a k_I} \quad \ldots (8)$$

The nonlinear model of the actuator system is now simulated and the results are shown in Fig. 15. The left half of the figure shows the step response of the actuator for a displacement command of 3mm, and the right half shows the response for a step displacement command of 30mm. The control voltage and motor current are also plotted in the figure. The 30mm step shows saturation of the control voltage at 24 volts for a relatively long duration. The current limit is set at 20 amperes. The smaller 3mm step does not cause the control voltage and drive current to saturate. Figure 16 compares the nonlinear actuator model with its linear transfer function approximation in Equation (8) for a 5mm displacement command step. The slight difference is due to the current and voltage saturations and the deadzone nonlinearity, which are absent in the linear approximation. The transfer function in Equation (8) is however seen to be quite a good approximation to the nonlinear model for small step commands.

5.0 ROBUST CONTROL DESIGN

5.1 H_∞ Loop-shaping design procedure

For controller design, we shall use the H_∞ loop-shaping design procedure described in Refs 9 and 14. The procedure is intuitive as it is based on the generalisation of classical loop-shaping ideas. The open-loop plant, once given the desired loop-shape, is robustly stabilised against coprime factor uncertainty. The resulting controller has been shown to enjoy some favourable properties, such as no pole-zero cancellation occurs in the closed-loop system (except for a certain special class of plants)[17]. In addition, the controllers thus designed have been successful in various applications; examples are those described in Refs (11,13,15,14). Robustness of the controller is an important requirement for our case as the dynamics of the re-entry vehicle vary considerably during its flight; the variations in Mach number and dynamic pressure are discussed in section 4.2.

In practical design applications, the performance specifications are first translated into the frequency domain, and the open-loop plant's frequency response is given the desired shape. This is achieved by augmentation of the nominal plant model $G(s)$ by a suitable compensator (or weighting function) $W(s)$. The shaped plant $G_s = GW$ is then

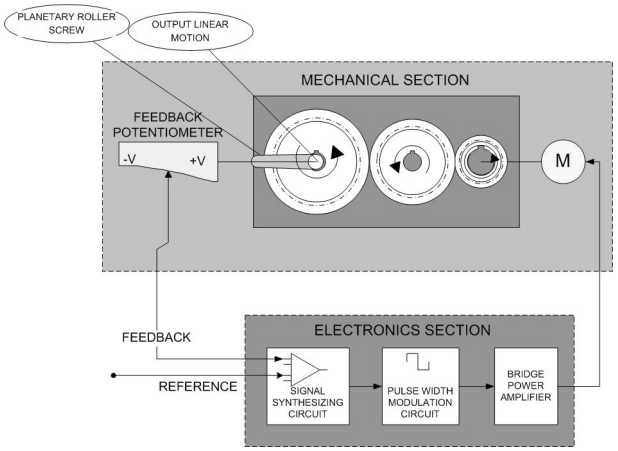


Figure 12. Actuator system schematic diagram.

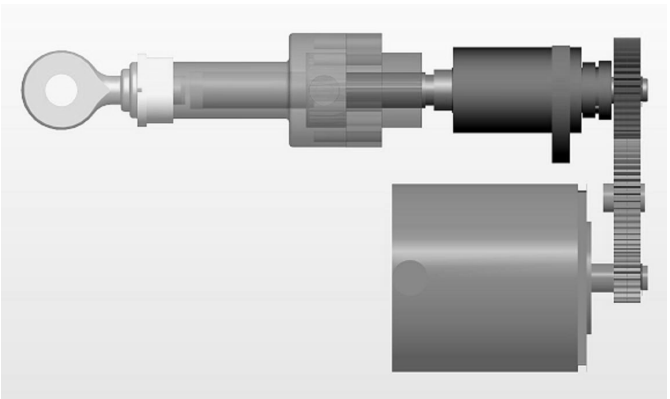


Figure 13. Actuator power transmission mechanism.

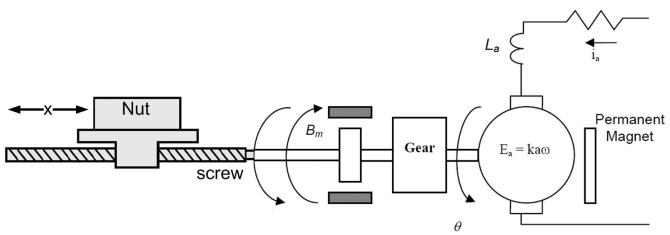


Figure 14. A simplified model of the actuator system.

robustly stabilised against coprime factor uncertainty, and the controller K_∞ thus obtained is cascaded with the weight W to obtain the final controller $K = WK_\infty$. It can be shown that the controller does not significantly alter the specified loop-shape provided a sufficiently small value of the cost γ is achieved, for details refer to Ref. 14).

We now outline a design procedure for designing controllers based on open-loop shaping and robust stabilisation of the normalised coprime factors of the plant. The procedure consists of the following main steps.

1. Plot the frequency response of the open-loop plant $G(s)$. Based on the desired bandwidth of the feedback loop, decide upon a crossover frequency for the open-loop transfer function.
2. Select a suitable weighting function $W(s)$ to give the plant a desired open-loop shape. The crossover frequency should be adjusted close to the desired bandwidth. Also $W(s)$ should be

https://doi.org/10.1017/S0001924000003699 Published online by Cambridge University Press

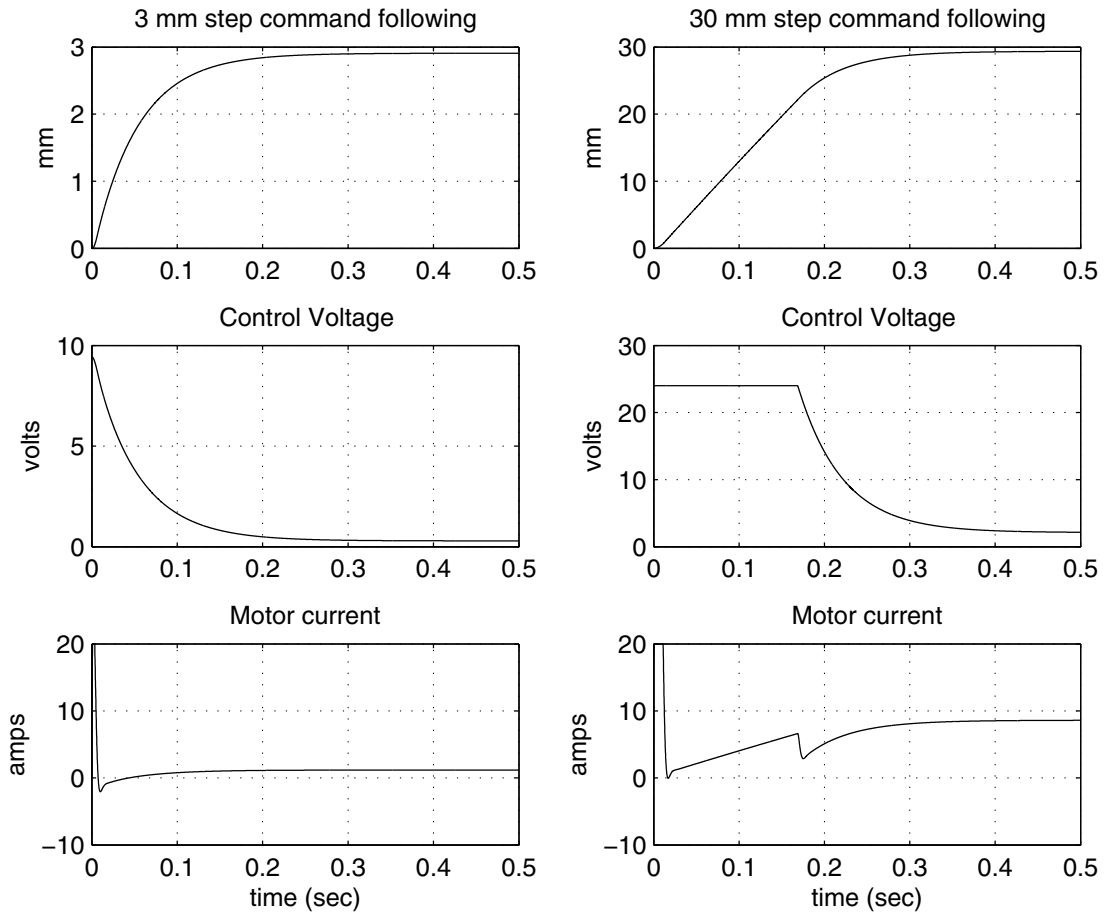


Figure 15. Nonlinear simulation of actuator system.

designed to give a roll-off of −1 (or −20dB/decade) at the crossover frequency. Build the shaped plant $Gs(s) = G(s)W(s)$ and calculate the optimal cost γ_{opt}[9]. A high value (typically > 10) of γ_{opt} indicates that the specified loop-shape is inconsistent with robust stability; in such a case the weighting function W should be modified.

3. Use a slightly sub-optimal value of γ and compute the corresponding controller K_∞.
4. Cascade the controller with the weight W to compute the final controller $K = WK_\infty$. Controller order reduction may be performed, if desired.
5. Form the closed-loop and check the appropriate performance and robustness measures against the given specification.

5.2 The plant model

The plant model consists of both the actuator and vehicle dynamical models in series. The actuator model relates the commanded pin position δ_{cref} to the actual pin position δ_c. The vehicle model relates the actual position of the pin-protuberance (H or δ_c) to the pitch attitude angle θ of the vehicle. Here we linearise the equations of motion of the vehicle around a particular flight condition, as given in Ref. 6. The flight condition chosen is Mach 3·5, velocity of 1,120ms^{-1}, and a dynamic pressure of 460kPa. This condition corresponds to that portion of the re-entry flight where the control authority of the pin-protuberance becomes appreciable. The actuator model is cascaded with the vehicle model to have the complete linearised dynamics of the plant for the given flight condition. This enables us to use the linear robust control theory presented above to design and implement a robust controller for this plant.

The complete plant model thus has δ_{cref} as its input and the pitch angle θ as its output. We assume that the pitch angle is a measured variable, there are standard sensors (gyroscopes) which can easily provide such a measurement†. The control system will therefore take in feedback measurements of θ, compare this with the reference or commanded pitch angle θ_c, and then actuate the pin-protuberance to drive this error to zero. As discussed previously in section 2, an outer guidance loop will also usually form part of the overall strategy. The guidance loop works on the feedback of position and velocity measurements, compares this to the desired trajectory, and generates pitch and yaw angle commands which the inner attitude control loops are designed to track. These pitch and yaw attitude variations cause angles-of-attack and sideslip to be generated, and these intermediate variables (α, β) are responsible for producing the lift force that guides the vehicle to the desired trajectory. It may be noted here that the pitch angle and not the angle of attack is used here for feedback, since it is difficult in practice to get reliable measurements of the latter. But since the outer guidance loop will be concurrently active, providing continuous attitude adjustment commands, this should not be a

†Gyroscopes are typically high bandwidth sensors, their dynamic response is considered fast and approximated by a constant gain here.

https://doi.org/10.1017/S0001924000003699 Published online by Cambridge University Press

problem. However, here we shall keep our focus on the design of the inner attitude control loop, since this fundamental capability needs to be established first before the higher level guidance logic can be deliberated upon.

5.3 Controller design

We now present the design of a robust controller following the procedure given in Section 5.1 above.

1. The frequency response of the open-loop plant $G(s)$ is plotted. A cross-over frequency of ~30rad/s is chosen for control design. This will yield a reasonable bandwidth for the closed-loop system.
2. A compensator (or weighting function) W is now selected. The weighting function chosen is:

$$W(s) = 80\left(\frac{3.162s + 27.6}{s + 87.28}\right)\left(\frac{s+1}{s+0.2}\right)$$

which is a lead-lag network with the gain adjusted to give the desired cross-over frequency. The lead gives suitable phase advance at cross-over, and the lag network boosts the low frequency gain to improve tracking and disturbance rejection at these frequencies. The frequency response of both the original plant G and the shaped plant $G_s = GW$ is shown in Fig. 17. The optimal cost value γ_{opt} is computed as 1·54.

3. A slightly sub-optimal γ of 1·63 is chosen (5% higher than the optimal), and the corresponding controller K_∞ computed.
4. The controller is cascaded with the weight W to form the overall controller $K = WK_\infty$.
5. The closed-loop system is formed, and the performance and robustness measures in terms of the sensitivity and the complementary sensitivity functions respectively, are plotted and checked; see Fig. 18. Both measures show adequate performance and robustness, with peak values less than 2·2dBs.

6.0 CONTROLLED FLIGHT SIMULATION RESULTS

The controller designed in the previous section is now implemented in the 6-DOF simulation to yield a closed-loop nonlinear flight simulation. A desired (or reference) pitch attitude profile is generated which we desire the vehicle to follow during flight. The actual pitch angle of the vehicle is fed back, so that an error signal is formed, which is to be minimised. This error signal becomes the input to the controller, which then actuates the pin-protuberance actuation mechanism (i.e., generates the δ_{cref} signal which drives the actuator) to reduce the pitch error to zero. The controller therefore, continuously modulates the pin height so that the actual pitch angle tracks the desired trajectory. The closed-loop simulation configuration is illustrated in Fig. 19.

The nonlinear closed-loop simulation results are now presented. The top part of Fig. 20 shows the perturbation in the nominal pitch profile of a particular re-entry trajectory. The nominal re-entry trajectory consists of the pitch angle Θ with a profile as shown in Fig. 10. The vehicle is controlled in the neighbourhood of the nominal trajectory. Figure 20 shows the commanded perturbation in the pitch angle with a dash-dot line, and the actual pitch angle θ with a solid line. The tracking performance of the controller is seen to be good; the actual angle follows the desired angle closely. The lower part of the figure shows the pin-protuberance height δ_c (or H) which is generated by the controller to track the reference pitch trajectory. The pin height varies from −10mm to +6mm for this particular case. Figure 21 shows the angle-of-attack α and the Mach number for the same simulation run. The decaying oscillations in the angle-of-attack profile indicate the natural stability of the vehicle (since the pin does

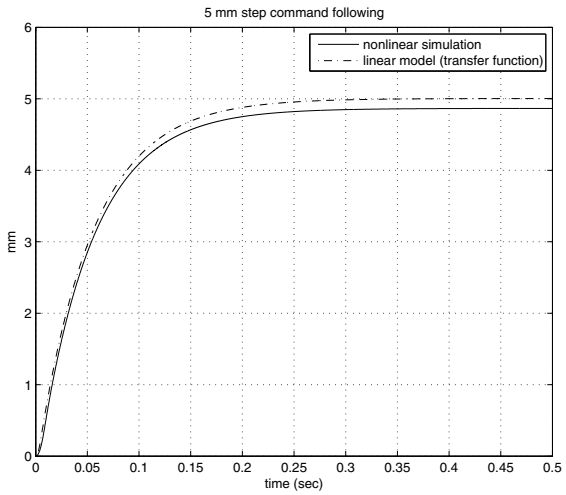


Figure 16. Actuator nonlinear and linear model comparison.

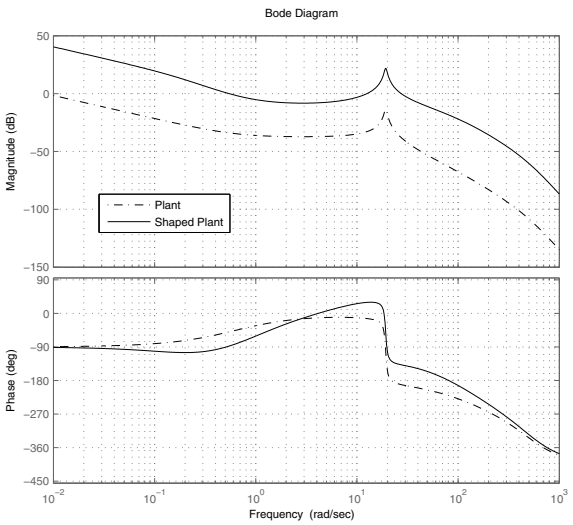


Figure 17. Frequency response of the original plant G and the shaped plant G_s.

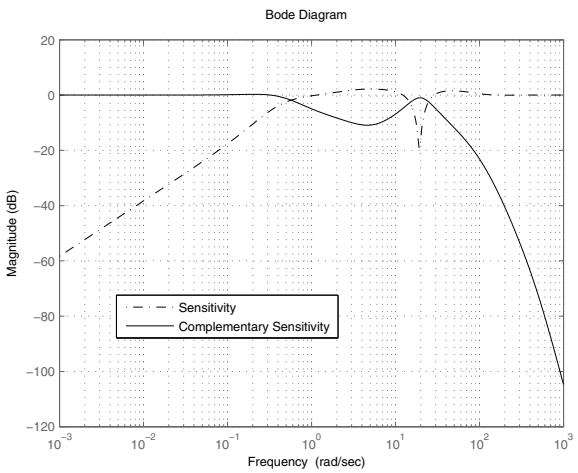


Figure 18. Magnitude plot of the Sensitivity and the Complementary Sensitivity functions.

https://doi.org/10.1017/S0001924000003699 Published online by Cambridge University Press

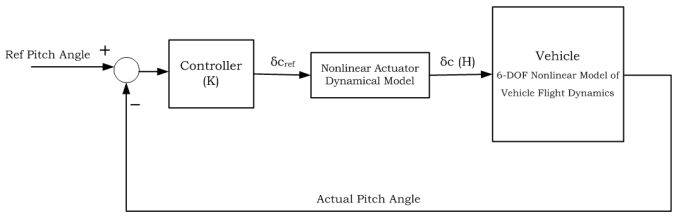


Figure 19. The closed-loop simulation configuration.

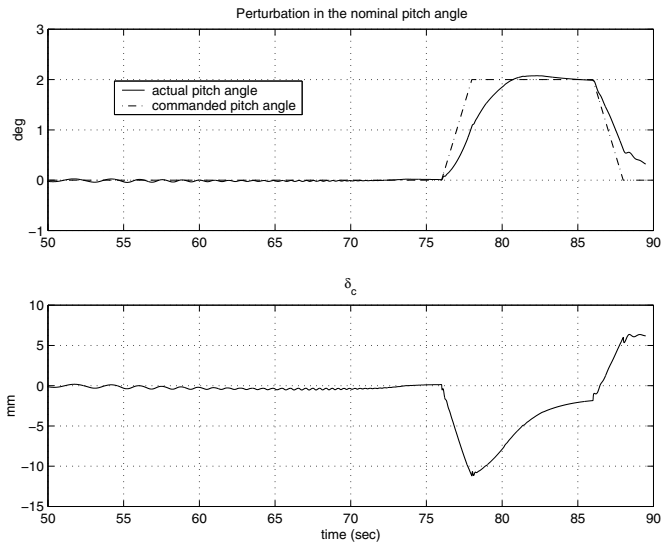


Figure 20. Tracking performance of the controller for a pitch command input.

not act during this time) as it reenters the atmosphere with an initial angle of attack of −5°; see the initial condition vector Equation (7). Since the vehicle is naturally stable, any angle of attack at re-entry will damp out automatically with zero control input. However when the pitch angle is commanded to maneuver away from the nominal pitch profile at 76 seconds, the controller actuates the pin to track the given pitch command, thus generating an angle of attack in the process. This capacity for generating an angle of attack can be utilised for providing lift for changing the path of the vehicle, i.e., for guidance.

Figures 22 and 23 show another simulation run with a different pitch command profile. Here the pitch angle is commanded to vary up to 8° from the nominal profile. The controller tracks this commanded profile by using a larger control input; the pin extension goes up to 26mm (the maximum possible value is 28·4mm) as seen from the lower part of Fig. 22. The tracking is seen to be satisfactory. The angle of attack generated in this case is larger, and goes to about 2° as seen in Fig. 23.

7.0 CONCLUSION

The control performance of a solid pin modelled as a variable extension is explored for a blunted, cone-shaped re-entry vehicle. The flow disturbance generated by the pin-protuberance is studied using CFD techniques at different Mach numbers, and for different extension settings. The overall pressure distribution around the vehicle is integrated to yield force and moment coefficients for different Mach number and angle-of-attack conditions, and with pin extensions varying from zero to twice the diameter of the pin. After quantification of the aerodynamic characteristics of the pin-protuberance, an

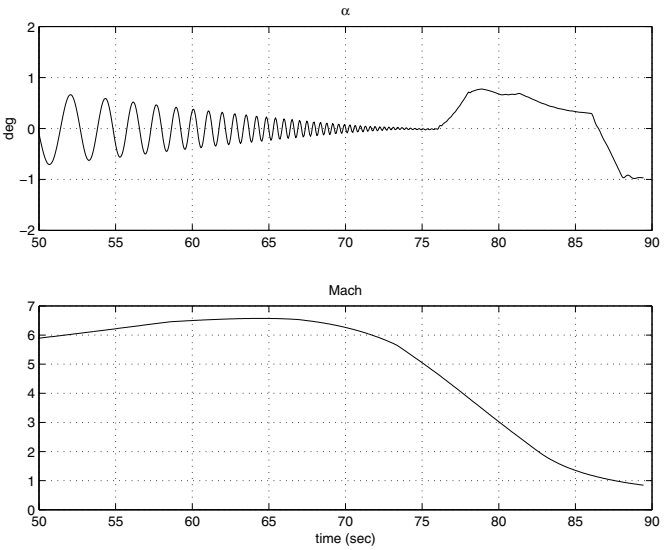


Figure 21. The angle of attack and the Mach number for the case in Fig. 20.

actuation mechanism design is presented that can provide a variable (and controlled) extension to the pin. The pin height H can therefore be continuously adjusted by giving appropriate commands to this actuation mechanism. A control system is then designed which controls the pitch attitude of the re-entry vehicle by a continuous adjustment of the pin height setting. The controller takes in sensed measurements of the pitch attitude, compares it with the desired attitude, and then drives the pin extension actuator to reduce the error to zero. The controller design is presented and then the 6-DOF nonlinear simulation results with the controller in the loop are shown. It is seen that the idea of trajectory control using the variable pin extension concept is a workable idea, and can be used to provide effective control of pitch attitude close to the nominal trajectory.

The concept of using a variable extension protuberance for trajectory control is both simple and inexpensive. The actuation mechanism is also straightforward in design and fabrication. This nevertheless also has limitations since arbitrarily large control moments cannot be generated; the pin extension is only useful when operating within the boundary layer. The maximum height of the pin that we use is therefore limited to twice its diameter. Also in this case the protuberance is seen to be effective for a particular Mach number range. If deemed necessary, this could be coupled with a speed control system which would keep the Mach number of the vehicle in the range where the pin-protuberance is most effective. The two controllers could then work in tandem, providing larger maneuvering capabilities.

REFERENCES

1. BLAKELOCK, J.H. *Automatic Control of Aircraft and Missile*, John Wiley & Sons, 2nd ed, 1991.
2. CASSEL, L.A., DURANDO, N.A., BULLARD, C.W. and KELSO, J.M. Jet interaction control effectiveness for subsonic and supersonic flight. Technical Report RD-TR-69-21, McDonnell Douglas Astronautics Company, 1969.
3. CHAMBERLAIN, R., MCCLURE, D. and DANG, A. CFD analysis of lateral jet interaction phenomena for the THAAD interceptor. In Proceedings of the 38th AIAA Aerospace Sciences Meeting & Exhibit, Reno, NV, USA, January 2000.
4. Aerodynamics Division. *A User's Guide to LOOK*. Aerodynamics and Structural Analysis Centre, Islamabad, Pakistan, 1997.
5. Aerodynamics Division. *A User's Guide to PAK-3D*. Aerodynamics and Structural Analysis Centre, Islamabad, Pakistan, 1998.

https://doi.org/10.1017/S0001924000003699 Published online by Cambridge University Press

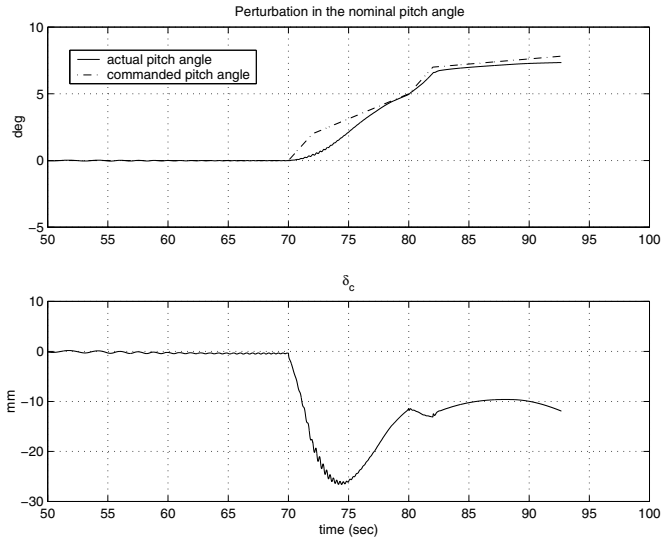


Figure 22. Tracking performance of the controller for another pitch command input.

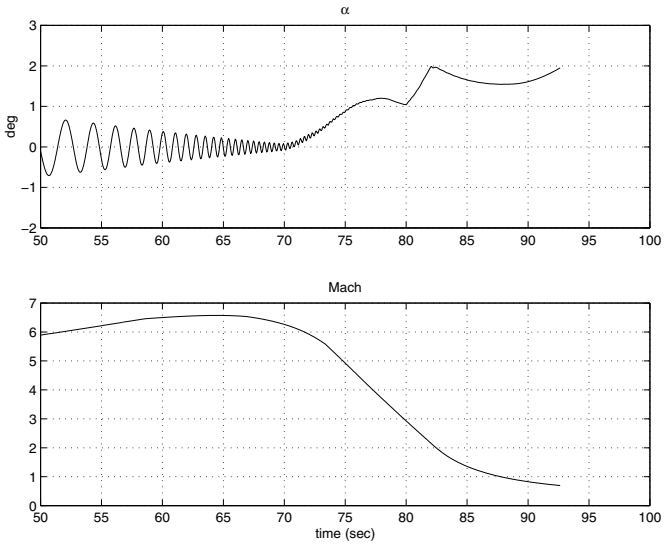


Figure 23. The angle of attack and the Mach number for the case in Fig. 22.

6. KANDEBO, S.W. New powerplant key to missile demonstrator, *Aviation Week and Space Technology*, September 2002, **157**, (10), pp 56–59.
7. MARX, W.J., WESSLING III, F.C., PETERS, B.R., THIES, A., STRICKLAND, B.R. and LIANOS. D. Miniature smart munitions/guided projectiles for the objective force. In 23rd Army Science Conference, December 2002.
8. MASSEY, K.C., MCMICHAEL, J., WARNOCK, T. and HAY, F. Development of mechanical guidance actuators for a supersonic projectile. *Aeronaut J*, April 2008, **112**, (1130), pp 181–195.
9. MCFARLANE, D. and GLOVER, K. A loop shaping design procedure using H_∞ synthesis, *IEEE Transactions on Automatic Control*, 1992, **37**, (6), pp 759–769.
10. MCRUER, D., ASHKENAS, I. and GRAHAM, D. *Aircraft Dynamics and Automatic Control*, Princeton Univeristy Press, Princeton, New Jersey, USA, 1973.
11. POSTLETHWAITE, I., PREMPAIN, E., TURKOGLU, E., TURNER, M.C., ELLIS, K. and GUBBELLS, A.W. Design and flight testing of various H_∞ controllers for the Bell 205 helicopter, *Control Engineering Practice*, 2005, **13**, pp 383–398.
12. REGAN, F.J. and ANANDAKRISHNAN, S.M. *Dynamics of Atmospheric Re-Entry*. AIAA Education Series. American Institute of Aeronautics and Astronautics, 1993, Washington DC, USA.
13. SAMAR, R., MURAD, G., POSTLETHWAITE, I. and GU, D.-W. A discrete time H_∞ observer-based controller and its application to a glass tube production process, *European J Control*, 1996, **2**, pp 112–125.
14. Skogestad, S. and Postlethwaite, I. *Multivariable Feedback Control Analysis and Design,* John Wiley & Sons, West Sussex, England, UK, 2nd ed, 2005.
15. SMERLAS, A., WALKER, D.J., POSTLETHWAITE, I., STRANGE, M.E., HOWITT, J. and GUBBELLS, A.W. Evaluating H_∞ controllers on the NRC Bell 205 fly-by-wire helicopter. *Control Engineering Practice*, 2001, **9**, (1), pp 1–10.
16. STEVENS, B.L. and LEWIS, F.L. *Aircraft Control and Simulation*, John Wiley & Sons, 1992.
17. TSAI, M.C., GEDDES, E.J.M. and POSTLETHWAITE, I. Pole-zero cancellations and closed-loop properties of an H_∞ mixed sensitivity design problem, *Automatica*, 1992, **28**, (3), pp 519–530.
18. WARNASH, A. and KILLEN, A. Low cost, high G, micro electromechanical (MEMS) inertial measurement unit (IMU) program. In 23rd Army Science Conference, December 2002.
19. ZAHIR, S. and ASIF, M. Computational aerodynamic interaction of a side plate and forward facing spike on blunted configurations in hypersonic flow. In Proceedings of the East West High Speed Flow Field Conference, Beijing, China, October 2005.
20. ZAHIR, S. and YE, Z. Aerodynamic analysis of pitched plate/jet – interactions with hypersonic flow. Czech Aerospace Proceedings, **2**, 2007.
21. ZAHIR, S. and YE, Z. Hypersonic flow interaction of pitched plates on blunted cone at incidence. *Int J Mathematical Models and Methods in Applied Sci*, 2007, **1**, (3), pp 133–136.
22. ZAHIR, S. and YE, Z. Hypersonic flow interaction of pitched short lateral plates on blunted cone configuration. In Proceedings of the 2nd European Conference for Aerospace Sciences, Brussels, Belgium, July 2007.
23. ZUBKOV, A.I., KUZNETSOV, O.M. and PANOV, Y.A. Vortices downstream of a wedge in a supersonic flow on a surface with a turbulent boundary layer, *J Fluid Dynamics*, 1996, **31**, (1).

https://doi.org/10.1017/S0001924000003699 Published online by Cambridge University Press